Topological spin-torque diode effect in skyrmion-based magnetic tunnel junctions

Bin Fang[1,7*], Riccardo Tomasello[2,7], Yuxuan Wu[1,3,7], Aitian Chen[4], Shuhui Liu[1,3], Baoshun Zhang[1], Emily Darwin[2], Mario Carpentieri[2], Wanjun Jiang[5], Xixiang Zhang[4], Giovanni Finocchio[6*] and Zhongming Zeng[1,3*]

[1]*Nanofabrication facility, Suzhou Institute of Nano-Tech and Nano-Bionics, Chinese Academy of Sciences, Suzhou, Jiangsu 215123, China*

[2]*Department of Electrical and Information Engineering, Politecnico di Bari, I-70125 Bari, Italy*

[3]*School of Nano Technology and Nano Bionics, University of Science and Technology of China, Hefei, Anhui 230026, People's Republic of China*

[4]*Physical Science and Engineering Division, King Abdullah University of Science and Technology, Thuwal 23955–6900, Saudi Arabia*

[5]*State Key Laboratory of Low-Dimensional Quantum Physics and Department of Physics, Tsinghua University, Beijing 100084, China.*

[6]*Department of Mathematical and Computer Sciences, Physical Sciences and Earth Sciences, University of Messina, I-98166 Messina, Italy.*

[7]*These authors contributed equally:* Bin Fang, Riccardo Tomasello, Yuxuan Wu

To whom correspondence should be addressed: bfang2013@sinano.ac.cn; gfinocchio@unime.it; zmzeng2012@sinano.ac.cn;

The growing market and massive use of Internet of Things nodes is placing unprecedented demands of energy efficient hardware for edge computing and microwave devices. In particular, magnetic tunnel junctions (MTJs), as main building blocks of spintronic microwave technology, can offer a path for the development of compact and high-performance microwave detectors. On the other hand, the fascinating field of skyrmionics is bridging together concepts from topology and spintronics. Here, we show the proof-of-concept of a topological spin-torque diode realized with an MTJ on top of a skyrmionic material at room temperature and for a wide region of applied fields, including the zero-field case. Our spin-torque diode electrical measurements show the electrical excitation of a skyrmion resonant mode with frequencies near 4 GHz and a selectivity one order of magnitude smaller than the uniform modes excited in the same device. Micromagnetic simulations identify these dynamics with the excitation of the breathing mode and point out the role of thickness dependent magnetic parameters (magnetic anisotropy field and Dzyaloshinkii–Moriya interaction) in both stabilizing and exciting the magnetic skyrmions. This work marks a milestone for the development of topological spin-torque diodes.

The electrical manipulation and detection of topological quasi-particles and phases are key aspects that can add functionalities at device level, impacting the enhancement of several emerging fields in condensed matter physics [1–7].

In the last years, the interest on magnetic skyrmions and skyrmionic phases has grown thanks to the study of their fundamental properties and their potential as building blocks for applications in magnetic storage[8–13] and reservoir, probabilistic and neuromorphic computing[14–18]. The rapid advancements and optimization of material development and nanofabrication for controlling and manipulating magnetic skyrmions[19–21] have opened up an exciting research direction in spintronics, in which the skyrmion electrical detection can be achieved in magnetic tunnel junctions (MTJs) via the tunneling magnetoresistive signal (TMR)[22]. In the industry-compatible CoFeB/MgO/CoFeB MTJ stack, the TMR signal related to skyrmions stabilized in the CoFeB free layer (FL) was first indirectly measured at low temperature[23], and then at room temperature[24]. Furthermore, the efforts to develop MTJ stacks to simultaneously perform imaging and electrical detection of skyrmions was successfully proved in a CoFeB/MgO/Ta/Co MTJ with engineered Dzyaloshinkii-Moriya interaction (DMI), where a TMR signal of 1.5% was achieved[25]. Currently, the primary strategy employed to enhance the electrical signal of a skyrmion is to combine multilayers hosting room temperature magnetic skyrmions[26–29] with an optimized MTJ. This approach has been effective in demonstrating the electrical detection of skyrmions with a TMR larger than 20%[30,31]. The previous experimental efforts focused mainly on the static properties of skyrmions. However, one of the next breakthroughs, namely the development of skyrmion-based computing and microwave technology, calls for the electrical detection of the skyrmion dynamics in MTJs which relies on the simultaneous excitation and detection of a skyrmion mode. In this way, by combining industry-compatible MTJs and topologically non-trivial magnetization textures, we could introduce topological magnetism into realistic applications, i.e. realize topological devices. Perpendicular MTJs stand as the most promising venue to accomplish this task. On one hand, the spin-torque diode (STD) effect in MTJs has proven effective for computing applications[32–34]. On the other hand, theoretical predictions on topological STDs promise high performance in microwave detection and energy harvesting[35]. The latter exploits internal dynamics of the skyrmion known as breathing modes[36]. Differently from other internal modes, i.e. clockwise (CW) and counterclockwise (CCW), the breathing mode can be excited via an out-of-plane field[37] and it has only been experimentally observed with skyrmion lattices in bulk materials at low temperature[38–40]. For skyrmion lattices in magnetic multilayers at room temperature, only signatures of the CW and CCW modes have been excited by an in-plane ac field[41,42].

Here, we establish a multilayer combining a skyrmionic material hosting skyrmions at room temperature with a perpendicular MTJ stack on top, similarly to a previous work[30]. The MTJ is designed so that the magnetostatic field from the skyrmionic material can transfer the skyrmion state into its FL. We have performed measurements of the spin-torque ferromagnetic resonance (ST-FMR) response in MTJs with a diameter smaller than 300 nm. We have studied the topological STD effect of a skyrmion as a function of the out-of-plane (OOP) field. We have also achieved the zero-field excitation after having stabilized zero field skyrmion by means of the application of an ad hoc field protocol. This is a scenario more relevant for applications. With full 3D micromagnetic simulations, we have identified the excitation of the skyrmion breathing mode as expected for MTJs with a perpendicular polarizer, which has a resonance frequency near 4 GHz. At large fields, we observe two modes, which are related to the excitation of uniform modes. Therefore, our work (i) demonstrates the first simultaneous electrical excitation and detection of the experimental microwave response of a magnetic skyrmion, and (ii) represents the experimental proof-of-concept of a topological STD. These results pave the way for future developments of topological devices, not only for skyrmion-based microwave technology, but also for other applications, such as computing[43] and non-trivial topological textures - hopfions[44,45].

Device description

The device stack is shown in Figure 1a. We use magnetron sputtering to grow magnetic films consisting of Ta (5)/CuN (20)/Ta (5)/[Pt (2.5)/Co (1)/Ta (0.5)]$_9$/Pt (2.5)/Co (1)/$Co_{40}Fe_{40}B_{20}$ (0.9)/MgO (0.85)/$Co_{20}Fe_{60}B_{20}$ (1.1)/Ta (0.5)/Co (0.3)/[Pt (1.5)/Co (0.4)]$_2$/Ru (0.85)/[Co (0.5)/Pt (1.5)]$_3$/Ru (5) – thicknesses in nm - on top of a thermally oxidized Si substrate. The $Co_{40}Fe_{40}B_{20}$ (0.9)/MgO (0.85)/$Co_{20}Fe_{60}B_{20}$ (1.1) is the part of the stack related to the MTJ (see Methods for more details on sample preparation). The top CoFeB is the perpendicularly magnetized reference layer (RL) pinned by a synthetic antiferromagnet (SAF) layer. The [Co (0.5)/Pt (1.5)]$_3$ acts as the hard layer (HL) and is used to enhance the coercive field. The bottom CoFeB acts as a FL and it is directly coupled with Pt (2.5)/Co (1)/Ta (0.5)]$_9$/Pt (2.5)/Co (1), i.e. the skyrmionic layer (SkyL), which allows for stabilizing magnetic skyrmions at room temperature for a wide range of magnetic fields. Using electron-beam lithography and ion milling, these films were patterned into MTJ devices with circular cross sections of diameters ranging from 100 nm to 500 nm. Figure 1b shows the scanning electron microscope (SEM) image for an MTJ with a diameter of 270 nm. We have also characterized the stack cross section using transmitting electron microscopy (TEM) to evaluate the quality of magnetic films, as shown in Figure 1c, which exhibits the uniform layered structure and sharp interface characteristics (see Supplementary Figure S1 for additional images). The inset of Figure 1c shows the detail of the MgO and the two adjacent CoFeB layers which highlights the quality of the tunnel barrier of the MTJ. Indeed, the MgO layer appears with a neat crystal phase arrangement giving rise to the TMR effect.

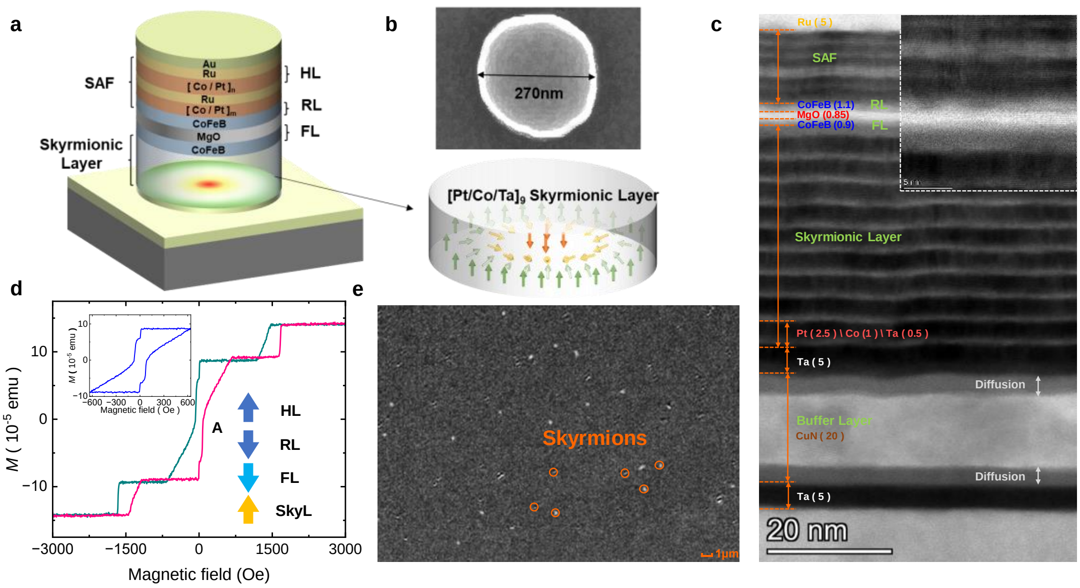

Figure 1. Device stack and experimental characterization. a, Schematic configuration of the device with the description of the films stack. The skyrmionic layer (SkyL), composed of [Pt/Co/Ta]$_9$, allows for the stabilization of magnetic skyrmions at room temperature. The CoFeB of the MTJ acting as the free layer (FL) is on top of the SkyL, while the reference layer (RL) is exchange biased by a SAF layer, HL is the hard layer. Both the FL and RL have a perpendicular easy axis. **b,** An SEM image of a patterned MTJ with a diameter of 270 nm. **c,** High resolution TEM (HRTEM) images of the whole stack. The HRTEM shows smooth

interfaces with an indication of the thickness of each layer (in nm). The inset is a magnification of the MgO barrier layer and points out its high crystalline quality. **d,** OOP magnetic field hysteresis major loop measured by vibrating sample magnetometry (VSM). The inset shows the corresponding minor loop. **e,** Polar MOKE magnetic imaging of the Ta/MgO/CoFeB/Ta/[Pt/Co/Ta]$_9$ stacks for an OOP field of 200 Oe showing isolated skyrmions. The OOP magnetization component is color coded: white is in the +z orientation. Scale bar, 1 μm.

Static characterization

Figure 1d shows an example of the OOP magnetic hysteresis loop for the thin films demonstrating the OOP easy axis, while the inset displays the minor loop with the change of the OOP field. The magnetic signal of the point A near zero field is marked by arrows of different colors, which correspond to that of the CoFeB/Ta/[Pt/Co/Ta]$_9$ multilayer. The magnetizations of the FL and the SkyL undergo antiferromagnetic coupling, as do the RL and the HL. The process of changing the relative magnetization direction between the FL and the RL is characterized by a step-shaped intermediate resistance state near zero magnetic field. To identify the magnetic configurations in this field region, we have performed magnetic imaging using polar magneto-optical Kerr effect (p-MOKE) microscopy (see the schematic of the measurement and the Kerr intensity magnetic-field loop in Supplementary Figure S2) in samples without the capping layer which are composed of the following stack [Ta(5)/MgO(0.85)/CoFeB(1.1)/Ta(0.5)/[Pt(2.5)/Co(1)/Ta(0.5)]$_9$. This is the same as the SkyL of the MTJ depicted in Figure 1a. When the external magnetic field is zero, the surface of the sample presents typical maze-shaped domains. With the gradual increasing of the magnetic field, the spin textures evolve from the maze-shaped domains into a configuration characterized by isolated skyrmions which micromagnetic simulations identify as pure Néel skyrmions (integer winding number). When the magnetic field is sufficiently large to saturate the magnetization, the skyrmions are annihilated (see Supplementary Figure S3 for a more detailed imaging of the field evolution of magnetic textures measured by p-MOKE). Figure 1e shows the spin texture at 200 Oe which is characterized by isolated skyrmions of around 250 nm diameter (the OOP magnetization components are color coded - white/black refers to +z/-z).

We refer to this intermediate state hosting isolated magnetic skyrmions at room temperature for a wide range of magnetic fields as a skyrmionic state.

Spin-torque diode measurements

We next study the rectification characteristics of the MTJ device for the skyrmionic and uniform states. We focus on MTJs with a diameter of 270 nm which is comparable to the maximum size of the skyrmions observed by p-MOKE microscopy. We use the circuit shown in Figure 2a for the ST-FMR measurements (see Methods for more details). The signal generator and source meter generate a microwave current $I_{ac} = I_{ac,0}\sin(2\pi f_{ac}t + \varphi)$ of frequency f_{ac}, phase φ and amplitude $I_{ac,0}$ and a direct current I_{dc}, respectively, which are applied to the MTJ device through a bias tee. We take advantage of the STD effect measuring the rectified voltage V_{dc} across the MTJ as a function of the microwave frequency f_{ac} to characterize the skyrmion modes. The rectified voltage depends on the amplitude of the microwave input, the amplitude of the MTJ oscillating resistance and the phase between them[46,47]. We have performed a systematic study of those modes as a function of the field amplitude and direction with respect to the out-of-plane axis characterized by the angle θ as defined in Figure 2a.

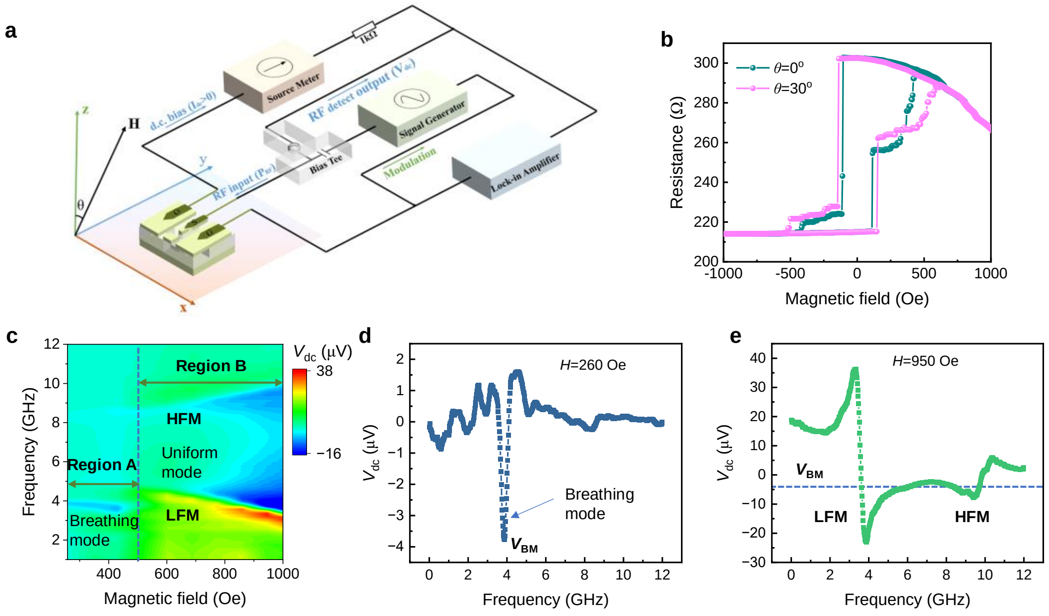

Figure 2. Magneto-electrical transport and ST-FMR characterization of the skyrmionic MTJ. a, Schematics of the circuit for the ST-FMR characterization, where a d.c. bias current is injected into the MTJ device by a DC terminal of the bias Tee. The differential voltage is

recorded by the lock-in amplifier. For the ST-FMR measurement, an RF current is injected by the signal generator, the rectified voltage is also recorded by a low frequency (97 Hz) modulation method using the lock-in amplifier. **b,** Magnetoresistance data measured as a function of magnetic field amplitude at $\theta = 0°$ and $\theta = 30°$, respectively, where θ is the angle between the normal and the magnetic field defined in panel **a**. The sharp change in the magnetoresistance curves indicates a switching process in the FL of the MTJ, while the gradual change can be linked to the skyrmionic region as observed in Figure 1d. **c,** ST-FMR spectra as a function of the amplitude of the external field for $\theta = 30°$ and $P_{\mathrm{rf}} = 5\mu\mathrm{W}$. The color code is linked to the value of the rectification voltage V_{dc}. Two regions are observed, region A is characterized by the excitation of the skyrmion breathing mode, while in region B, the excitation of the uniform modes for the FL and RL can be observed. **d, e,** Examples of ST-FMR measurements as a function of the microwave frequency ($\theta = 30°$ and $P_{\mathrm{rf}} = 5\mu\mathrm{W}$) for region A at $H = 260$ Oe and region B at $H = 950$ Oe, respectively.

To identify the field region where the skyrmionic state is stable, we first measured the magnetoresistance as a function of the field amplitude for different field angles θ. Figure 2b compares the results for $\theta = 0$ and 30° (similar curves are observed for other field angles as illustrated in the Supplementary Figure S4a and S4b for $\theta = 20°$ and 40°). The direction of the RL is set along the -z direction, hence for negative fields the antiparallel state (AP) with a large resistance is stabilized. As the field increases, we observe a jump from the parallel (P) state to the skyrmionic state, similar to the process identified in Figure 1e. The offset in the hysteresis loop is given by the dipolar field from the SAF layer, which is not totally compensated. At large enough magnetic fields $H = 550$ Oe, the AP state is stabilized. The reduction of the resistance of the AP state as the field keeps increasing is due to the rotation of the SAF layer magnetization, which, as can be observed, is a reversible process. A similar response is observed for the descending branch of the hysteresis loop while the magnetic field is decreasing, but not after the P state is achieved, the resistance remains constant up to at least -1000 Oe.

Then, we experimentally characterized the rectification voltage V_{dc} by measuring the ST-FMR spectra as a function of the field amplitude for the ascending branch of the hysteresis loop. Figure 2c summarizes the data for fields larger than 250 Oe, $\theta = 30°$ and $P_{\mathrm{rf}} = 5\mu\mathrm{W}$. We identify two different regions, A and B. In region A, where the skyrmionic state is stable, a single mode with a frequency near 4 GHz is excited. Its frequency slightly decreases as a function of the field amplitude. Figure 2d shows an example of the rectified voltage as a function of the microwave frequency for H = 260 Oe. It is characterized by a negative voltage peak and a narrow bandwidth. The fact that the MTJ FL is in the skyrmionic state and the magnetization of the RL is perpendicular allows us to infer that, in region A, the skyrmion breathing mode[35,36] is excited. As a first confirmation, the ST-FMR characterization of a conventional MTJ without the SkyL does not exhibit the mode in region A (see Supplementary Figure S5). Furthermore, micromagnetic simulations show the excitation of the breathing mode, as discussed in the next paragraph.

When the field increases, a transition from region A to B occurs. Here, two modes, a low frequency mode (LFM) and a high frequency mode (HFM) starting near 5 GHz and 8 GHz at H = 600 Oe are detected. The frequency of the LFM (HFM) decreases (increases) with the field. Figure 2e displays the rectified voltage as a function of the microwave input frequency for H = 950 Oe, as an example. In this field range, the MTJ is in the AP uniform state (see hysteresis loop in Figure 2b), therefore the HFM is related to the FL resonance mode, which is parallel to the applied field, while the LFM is linked to the RL resonance mode which is antiparallel to the field. Similar rectification curves are observed for different samples with the same nominal geometry and for a wide range input rf power up to 50 μW (see Supplementary Figure S6).

A direct comparison of the rectification curves for different modes shows that the maximum rectified voltage $V_{BM,}$ indicated in Figures 2c and d of the skyrmion breathing mode is smaller but of the same order of the one related to the excitation of the uniform mode. The resonant curve has a bandwidth of 163 MHz which is smaller as compared to 527 and 248 MHz for the HRM and LRM, respectively. This gives rise to a better selectivity which is a key element for the design of compact microwave detectors without the need of microwave filters.

We wish to add that the MTJ size, i.e. 270 nm in diameter, exhibited the largest ST-FMR signal related to the excitation of the skyrmion mode in the ground state of the FL hosting a single skyrmion with size comparable with the MTJ cross section. The ST-FMR data in MTJs with smaller diameter that we have measured do not exhibit this breathing mode, at the same time, the ST-FMR signal measured for larger MTJs is smaller (see Supplementary Figure S7 for the characterization of magnetoresistance and ST-FMR data for MTJ devices having diameter of 180 and 420 nm).

The ST-FMR spectra for $\theta = 20$ and 40° are also shown in Supplementary Figure S4c and S4d. For both field directions, the excitation of the breathing mode can be also observed.

Topological spin-torque diode at zero field

Technologically, it is more relevant to design a STD at zero field in order to reduce both the energy consumption and improve the scalability. The previous topological STD response is observed in many samples with the same nominal geometry, and, in some of them, also at zero field. The stabilization of zero field skyrmion is achieved via the application of a field protocol (see inset in Fig. 3a) similar to Ref.[48]. The main panel of Fig. 3a displays the corresponding magnetoresistance response. As the field decreases, the magnetoresistance at zero field decreases up to 140 Ω for field amplitudes lower than 10 Oe (see dark blue loop in Fig. 3a). This resistance value is very close to that one at the first jump of the magnetoresistance (H=110 Oe) for the two loops with field amplitude larger than 10 Oe, thus pointing out the stabilization of a zero field skyrmionic state.

Figure 3b shows the zero field ST-FMR spectrum related to the skyrmionic state. We notice that it is qualitatively different from those under the presence of the field. In particular, here the rectified voltage due to the breathing mode exhibits both a positive (3 μV) and a negative peak (-1 μV) around 2 GHz. We ascribe this behavior to the change of the phase between the magnetoresistance signal and the injected ac current I_{ac}.

The inset of Fig. 3b shows the linear dependence of the maximum value of the positive peak of the rectified voltage vs the input rf power. The zero field ST-FMR spectra for different input rf powers are illustrated in Supplementary Figure S8.

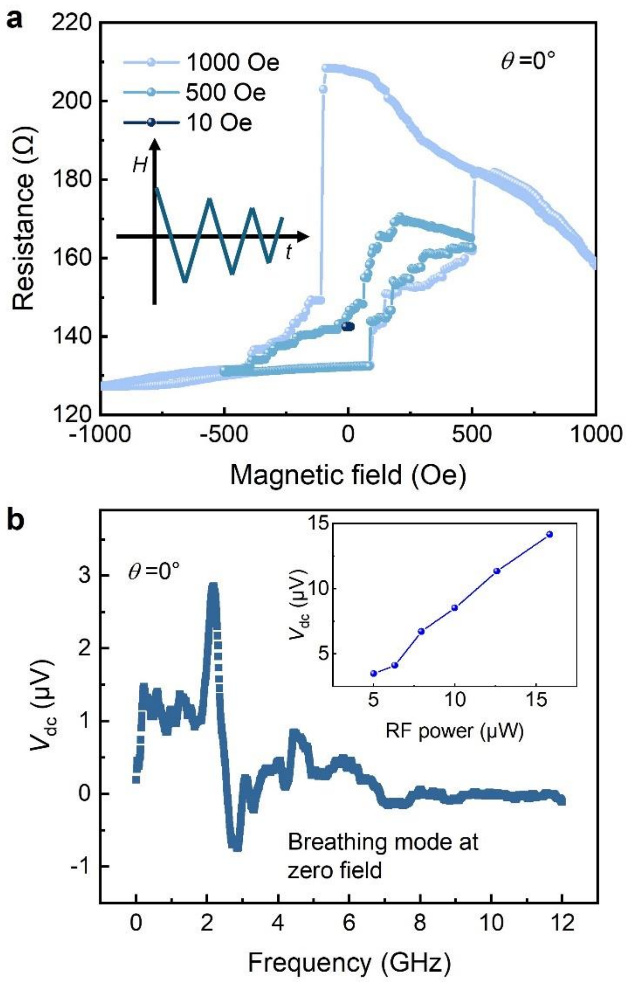

Figure 3. Zero field skyrmionic state. a, Magnetoresistance data measured as a function of a the field protocol (a time-varying magnetic field) necessary to achieve a zero field skyrmionic state at $\theta = 0°$. The inset shows the qualitative time-dependence of the magnetic field. **b**, Zero field ST-FMR measurements as a function of the microwave frequency ($\theta = 0°$ and $P_{rf} = 5$ μW). The inset shows the maximum value of the positive peak of the rectified voltage as a function of the input rf power.

Discussion

To corroborate the experimental results and achieve a more detailed understanding of the modes excited in the MTJ, we perform micromagnetic simulations based on the numerical integration of the Landau-Lifshitz-Gilbert equation. This includes the spin-transfer torque applied to both the FL and RL of the MTJ and the layer dependence of the magnetic parameters to reflect the different material compositions of the stack (see Methods).

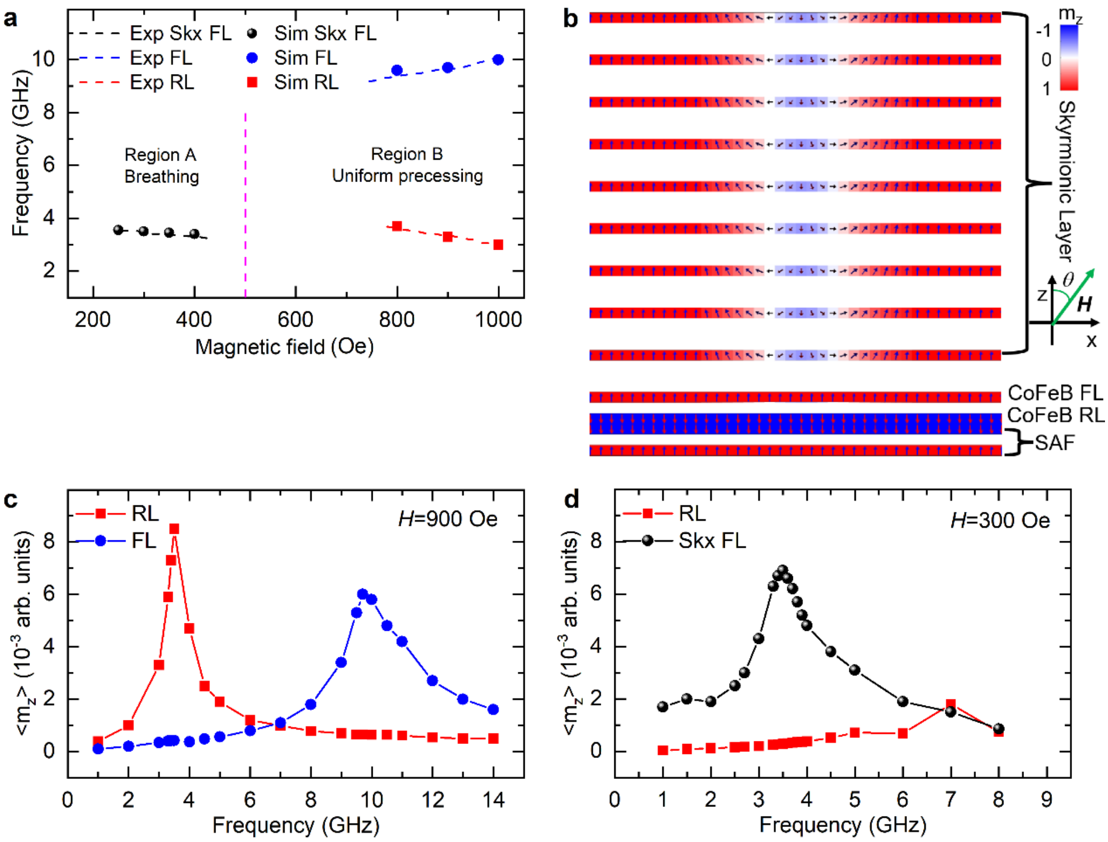

Figure 4. Micromagnetic simulations results. a, Frequency of the excited modes as a function of the applied field ***H*** for θ = 30°. Solid symbols represent the results of the micromagnetic simulations, dashed lines correspond to the experimental results extracted from Figure 2c. **b,** Cross-section of the simulated MTJ with the SkyL, where the initial state is a tubular Néel skyrmion (the color bar indicates the OOP component of the magnetization, the arrows indicate the direction of the magnetization in the x-z plane). The magenta dashed line divides region A where the skyrmion breathing mode occurs, from region B, where the uniform precession of both FL and RL is excited. **c**, Example of the frequency response for the FL and RL in the uniform AP state for *H*=900 Oe. **d**, Example of the frequency response for the FL and RL in the skyrmionic state for *H*=300 Oe.

Figure 4a shows a comparison between the frequency modes measured experimentally (dashed lines), already shown in Figure 2c, and the results of micromagnetic simulations (solid symbols). For large OOP fields *H*≥800 Oe, both magnetizations of the FL and RL are uniform, with the one in the FL aligned along the positive z-axis parallel to the applied field, and the one of the RL pointing in the opposite direction (AP state). The micromagnetic simulations are in quantitative agreement with the experimental data and thus confirm the link of the HFM and LFM with the resonant mode of the FL and RL, respectively. In detail, the HFM with the blue-shift is excited into the FL, while the LFM exhibiting the red-shift is related to the RL dynamics.

At smaller field 200<H<600 Oe, a single mode is observed. In order to understand its origin, we have studied the static characteristics of the skyrmionic state for a wide range of parameters. Experimentally (see Figure 2b) in this field region, both the uniform and the skyrmion state can be stabilized according to the field history. The theoretical details of the existence of this bi-stability region can be understood with theories published previously[49].

To describe the mode in region A, a tubular pure Néel skyrmion is set as the initial state in the SkyL (see Figure 4b), as suggested by the appearance of the intermediate states in the ascending branch of the hysteresis loop in Figure 2c. Whereas, FL, RL and SAF layers are considered in a uniform state. The calculation of the equilibrium configuration of the magnetization reveals that a Néel skyrmion is also nucleated in the CoFeB FL via the magnetostatic interaction from the skyrmionic state. This aspect is crucial to understand the reason why it can be detected electrically. This equilibrium state was used as the initial state for the micromagnetic frequency response analysis, where we use as input a microwave spin-polarized current. The micromagnetic simulations are again in agreement with the experimental results and shows the excitation of the breathing mode also exhibiting a slight red-shift. Our calculations also show that the red shift is due to the interaction of the skyrmion domain wall with the MTJ boundary. Figure 4c and d depict the magnetization amplitude as a function of the input frequency for the FL and RL in the uniform AP state (c) and with the FL in the skyrmionic state (d), respectively. The skyrmion breathing mode amplitude is slightly larger than the one of the uniform FL (black curve in d vs blue curve in c). However, the clear difference concerns the RL. The amplitude of this mode is much larger in the uniform precession, in agreement with the experimental data (a small amplitude RL mode in region A red curve in d which is observed in simulations can be also seen as weak mode in Fig. 2c).

Summary and Conclusions

In summary, we have developed a topological STD with sub-300 nm MTJs combining a SkyL able to host skyrmions at room temperature and a TMR stack. ST-FMR measurements reveal the excitation of the breathing mode of a skyrmion that, for our devices, exhibits a resonance frequency near 4 GHz in a region of applied fields. We have also demonstrated the topological STD effect at zero field after applying a proper field protocol to stabilize zero-field skyrmions. Micromagnetic simulations support quantitatively the experimental evidence.

Our work not only shows the proof of concept of the first topological STD and initiates the development of skyrmion-based microwave technology, but also opens up the accomplishment of promising perspectives. The ST-FMR due to the skyrmion mode exhibits a narrower bandwidth compared to the uniform precession in the same device, thus suggesting a path toward the design of highly-selective microwave detectors. Our results also call for the integration of skyrmionic materials hosting smaller skyrmions (i.e. materials with larger DMI), with state-of-the-art TMR stacks for scaling the size of the topological diodes and enhancing the detection sensitivity increasing the TMR ratio.

This work is a breakthrough in the intriguing research direction aiming to move topological materials into device concepts and it is expected to have an impact in future engineering applications and developments in the field of spintronics and hybrid CMOS-spintronic technology.

Methods

Sample preparation. The skyrmionics MTJ devices studied here were patterned from a (thermal silicon oxide substrate)/ Ta (5)/CuN (20)/Ta (5)/[Pt (2.5)/Co (1)/Ta (0.5)]$_9$/Pt (2.5)/Co (1)/$Co_{40}Fe_{40}B_{20}$ (0.9)/MgO (0.85)/$Co_{20}Fe_{60}B_{20}$ (1.1)/Ta (0.5)/Co (0.3)/[Pt (1.5)/Co (0.4)]$_2$/Ru (0.85)/[Co (0.5)/Pt (1.5)]$_3$/Ru (5) multilayer, deposited by using a Singulus TIMARIS physical vapor deposition system (thickness in nm). The 0.5 nm thick Ta dusting layer was inserted between $Co_{20}Fe_{60}B_{20}$ and Co (0.3)/[Pt (1.5)/Co (0.4)]$_2$ layers to enhance the perpendicular magnetic anisotropy (PMA) of the top reference layers. Here a CuN layer was used as a buffer layer for the growth of the MTJ stack. This skyrmionic MTJ multilayer was post-annealed at 300 °C without a magnetic field for 1 hour to enhance the TMR ratio and PMA property. The films were subsequently patterned into nanopillars using optical and electron beam lithography combined with ion milling, incorporating an MgO barrier targeting a resistance-area product (R×A) of 12.3 $\Omega\mu m^2$ in the parallel magnetization configuration. The patterned electrodes, Ti

(10 nm) and Au (100 nm), were fabricated using a lift-off process.

Magnetoresistance and ST-FMR measurements. All measurements reported in this paper are performed at room temperature. When the magnetoresistance was measured, a weak d.c. current I_{dc} was applied to the device through a bias Tee using a source meter (2400, Keithley), the voltage of the device was recorded by a nanovolt meter (2182, Keithley). The out-of-plane TMR ratio, defined as $(R_{AP}-R_P)/R_P$, was 39.5%. When a microwave current I_{ac} with a frequency f_{ac} was applied to the device through a bias Tee using a signal generator (N5183B), the free layer magnetization starts to precess at the same frequency, resulting in a time-dependent resistance oscillation due to the TMR effect. As a result, a rectified voltage is generated across the MTJ. To improve the signal-to-noise ratio, the microwave input was modulated at a low frequency (97 Hz), and the resulting rectified voltage V_{dc} was measured with a lock-in amplifier (SR830, Standard Research Systems).

Micromagnetic simulations. PETASPIN, an in-house CUDA-native full micromagnetic solver, was used to perform the micromagnetic simulations. This tool numerically integrates the Landau-Lifshitz-Gilbert (LLG) equation by applying the time solver scheme Adams-Bashforth[50]:

$$\frac{d\mathbf{m}}{d\tau} = -(\mathbf{m} \times \mathbf{h_{eff}}) + \alpha_{\mathrm{G}}\left(\mathbf{m} \times \frac{d\mathbf{m}}{d\tau}\right) \quad (1)$$

where $\mathbf{m} = \mathbf{M} / M_S$ is the normalized magnetization, α_G is the Gilbert damping, and $\tau = \gamma_0 M_S t$ is the dimensionless time, which uses γ_0 the gyromagnetic ratio and M_S the saturation magnetization. The normalized effective magnetic field, $\mathbf{h_{eff}}$, includes the exchange, interfacial DMI, magnetostatic, anisotropy and external fields.

The experimental MTJ is modelled as a circular stack with a diameter of 300 nm. The [Pt(2.5 nm)/Co(1 nm)/Ta(0.5 nm)]9 SkyL is simulated by nine repetitions of a 1 nm thick Co ferromagnet separated by a 3 nm thick Ta/Pt non-magnetic layer. The CoFeB FL (0.9 nm) and CoFeB (1.1 nm) in the RL are simulated by a 1 nm thick ferromagnetic layer each. These two CoFeB layers are separated by a 1 nm thick non-magnetic layer corresponding to the experimental MgO layer (0.85 nm). The CoFeB layer in the RL is in contact with the $[Co/Pt]_n/Ru/[Co/Pt]_m$ SAF layer. We modelled the latter as standard SAF composed of two 1 nm thick ferromagnetic layers separated by a 1 nm thick non-magnetic layer. The SAF stack is characterized by the interlayer exchange coupling (IEC) of the Ruderman–Kittel–Kasuya–Yosida (RKKY) type, with an effective field of $\boldsymbol{h}_{\mathrm{IEC},i} = \frac{J_{\mathrm{IEC}}}{\mu_0 M_{s,i}^2 t_{\mathrm{NM}}} \boldsymbol{m}_j$,[51,52] where i,j are the indices of the top and bottom layers of the SAF, respectively, J_{IEC} is the IEC constant, and t_{NM} is the thickness of the Ru spacer. We apply an OOP external field $\boldsymbol{H}$ tilted of θ with the respect to the z-axis. We use a cuboidal discretization cell of 3×3×1 nm^3.

For the excitation of the magnetization dynamics both in the FL and RL, we rely on the spin-transfer torque (STT) mechanism, which includes the effect of the back torque[53] on the RL magnetization due to an AC current $I_{ac} = I_{ac,0} \sin(2\pi f t + \varphi)$ of frequency f, phase φ and amplitude $I_{ac,0}$. The STT term is added to Eq. (1) as:

$$\begin{cases} \boldsymbol{\tau}_{STT-FL} = \dfrac{gP\mu_B}{\gamma_0 e M_{s-FL}^2 V_{FL}} I_{ac}[\boldsymbol{m}_{\mathrm{FL}} \times (\boldsymbol{m}_{\mathrm{FL}} \times \boldsymbol{m}_{\mathrm{RL}})] \\ \boldsymbol{\tau}_{STT-RL} = -\dfrac{gP\mu_B}{\gamma_0 e M_{s-RL}^2 V_{RL}} I_{ac}[\boldsymbol{m}_{\mathrm{RL}} \times (\boldsymbol{m}_{\mathrm{RL}} \times \boldsymbol{m}_{\mathrm{FL}})] \end{cases} \qquad (2),$$

where $\boldsymbol{m}_{FL}$ refers to the FL and $\boldsymbol{m}_{RL}$ to the RL. P is the spin-polarization equal to 0.66, μ_B is the Bohr magneton, g is the Landè factor, e the electron charge, and $V_{FL(RL)}$ is the volume of the FL (RL).

For the Co ferromagnets in the [Pt(2.5 nm)/Co(1 nm)/Ta(0.5 nm)]$_9$ SkyL, we considered M_s = 900 kA/m[30], perpendicular anisotropy constant K_u = 0.85 MJ/m^3, and interfacial DMI constant D = 2.2 mJ/m^2.

For the CoFeB FL and RL, as well as for the SAF layers we fix M_s = 1200 kA/m. The perpendicular anisotropy constants of the FL and RL are extracted by fitting the experimental frequency vs. field response in Figure 2c for the FL and RL uniform precessing (applied fields from 800 to 1000 Oe) by means of the well-known Kittel expression $f_{\mathrm{Kit}} = \frac{\gamma_0}{2\pi}\left(H_{\mathrm{ext}} + H_{K,\mathrm{eff}}\right)$, where $H_{K,\mathrm{eff}}$ is the effective magnetic anisotropy field. We obtain $K_{\mathrm{U,FL}} = 1.04$ MJ/m^3 and $K_{\mathrm{U,RL}} = 0.99$ MJ/m^3 for the FL and RL, respectively. The interfacial DMI of the FL is fixed to 1.1 mJ/m^2 (large enough to stabilize a Néel skyrmion),[54] while a zero DMI is considered for the RL and SAF layers. $K_{\mathrm{U,RL}}$ is also used for the perpendicular anisotropy constant of the SAF layers. In addition, we used an antiferromagnetic J_{IEC} = -0.5 mJ/m^2 which is sufficiently large to maintain the SAF in the antiferromagnetic state under the application of the OOP external field. All the simulations are performed at zero temperature.

References

1. Finocchio, G., Büttner, F., Tomasello, R., Carpentieri, M. & Kläui, M. Magnetic skyrmions: from fundamental to applications. *J. Phys. D. Appl. Phys.* **49**, 423001 (2016).
2. Li, J. *et al.* Topological liquid diode. *Sci. Adv.* **3**, 19–25 (2017).
3. Fert, A., Reyren, N. & Cros, V. Magnetic skyrmions: advances in physics and potential applications. *Nat. Rev. Mater.* **2**, 17031 (2017).
4. Bonanno, G. *et al. Magnetic Skyrmions and Their Applications* (eds. Finocchio, G. & Panagopoulos, C., Elsevier, 2021). doi:10.1016/B978-0-12-820815-1.09992-2.
5. Göbel, B., Mertig, I. & Tretiakov, O. A. Beyond skyrmions: Review and perspectives of alternative magnetic quasiparticles. *Phys. Rep.* **895**, 1–28 (2021).
6. Gilbert, M. J. Topological electronics. *Commun. Phys.* **4**, 70 (2021).
7. Dohi, T., Reeve, R. M. & Kläui, M. Thin Film Skyrmionics. *Annu. Rev. Condens. Matter Phys.* **13**, 73–95 (2022).
8. Sampaio, J., Cros, V., Rohart, S., Thiaville, A. & Fert, A. Nucleation, stability and current-induced motion of isolated magnetic skyrmions in nanostructures. *Nat. Nanotechnol.* **8**, 839–844 (2013).
9. Tomasello, R. *et al.* A strategy for the design of skyrmion racetrack memories. *Sci. Rep.* **4**, 6784 (2014).
10. Jiang, W. *et al.* Blowing magnetic skyrmion bubbles. *Science* **349**, 283–286 (2015).
11. Woo, S. *et al.* Observation of room-temperature magnetic skyrmions and their current-driven dynamics in ultrathin metallic ferromagnets. *Nat. Mater.* **15**, 501–506 (2016).
12. Jiang, W. *et al.* Direct observation of the skyrmion Hall effect. *Nat. Phys.* **13**, 162–169 (2017).
13. He, B. *et al.* All-Electrical 9-Bit Skyrmion-Based Racetrack Memory Designed with Laser Irradiation. *Nano Lett.* **23**, 9482–9490 (2023).
14. Grollier, J. *et al.* Neuromorphic spintronics. *Nat. Electron.* **3**, 360–370 (2020).
15. Song, K. M. *et al.* Skyrmion-based artificial synapses for neuromorphic computing. *Nat.*

Electron. **3**, 148–155 (2020).

16. Li, S. *et al.* Magnetic skyrmions for unconventional computing. *Mater. Horizons* **8**, 854–868 (2021).

17. Zázvorka, J. *et al.* Thermal skyrmion diffusion used in a reshuffler device. *Nat. Nanotechnol.* **14**, 658–661 (2019).

18. Raab, K. *et al.* Brownian reservoir computing realized using geometrically confined skyrmion dynamics. *Nat. Commun.* **13**, 6982 (2022).

19. Xu, T. *et al.* Imaging the spin chirality of ferrimagnetic Néel skyrmions stabilized on topological antiferromagnetic Mn3Sn. *Phys. Rev. Mater.* **5**, 084406 (2021).

20. Mandru, A.-O. *et al.* Coexistence of distinct skyrmion phases observed in hybrid ferromagnetic/ferrimagnetic multilayers. *Nat. Commun.* **11**, 6365 (2020).

21. Liu, J. *et al.* Manipulation of Skyrmion by Magnetic Field Gradients: A Stern–Gerlach-Like Experiment. *Nano Lett.* **23**, 4931–4937 (2023).

22. Ikeda, S. *et al.* A perpendicular-anisotropy CoFeB–MgO magnetic tunnel junction. *Nat. Mater.* **9**, 721–724 (2010).

23. Penthorn, N. E., Hao, X., Wang, Z., Huai, Y. & Jiang, H. W. Experimental Observation of Single Skyrmion Signatures in a Magnetic Tunnel Junction. *Phys. Rev. Lett.* **122**, 257201 (2019).

24. Kasai, S., Sugimoto, S., Nakatani, Y., Ishikawa, R. & Takahashi, Y. K. Voltage-controlled magnetic skyrmions in magnetic tunnel junctions. *Appl. Phys. Express* **12**, 83001 (2019).

25. Li, S. *et al.* Experimental demonstration of skyrmionic magnetic tunnel junction at room temperature. *Sci. Bull.* **67**, 691–699 (2022).

26. Moreau-Luchaire, C. *et al.* Additive interfacial chiral interaction in multilayers for stabilization of small individual skyrmions at room temperature. *Nat. Nanotechnol.* **11**, 444–448 (2016).

27. Soumyanarayanan, A. *et al.* Tunable room-temperature magnetic skyrmions in Ir/Fe/Co/Pt multilayers. *Nat. Mater.* **16**, 898–904 (2017).

28. Li, W. *et al.* Anatomy of Skyrmionic Textures in Magnetic Multilayers. *Adv. Mater.* **31**, 1807683 (2019).

29. Wang, Z. *et al.* Thermal generation, manipulation and thermoelectric detection of skyrmions. *Nat. Electron.* **3**, 672–679 (2020).

30. Guang, Y. *et al.* Electrical Detection of Magnetic Skyrmions in a Magnetic Tunnel Junction. *Adv. Electron. Mater.* **9**, 2200570 (2023).

31. Chen, S. *et al.* All-electrical skyrmionic magnetic tunnel junction. *Nature* **627**, 522–527 (2024).

32. Cai, J. *et al.* Voltage-Controlled Spintronic Stochastic Neuron Based on a Magnetic Tunnel Junction. *Phys. Rev. Appl.* **11**, 034015 (2019).

33. Cai, J. *et al.* Sparse neuromorphic computing based on spin-torque diodes. *Appl. Phys. Lett.* **114**, 192402 (2019).

34. Leroux, N. *et al.* Radio-Frequency Multiply-and-Accumulate Operations with Spintronic Synapses. *Phys. Rev. Appl.* **15**, 034067 (2021).

35. Finocchio, G. *et al.* Skyrmion based microwave detectors and harvesting. *Appl. Phys. Lett.* **107**, 262401 (2015).

36. Kim, J.-V. *et al.* Breathing modes of confined skyrmions in ultrathin magnetic dots. *Phys. Rev. B* **90**, 064410 (2014).

37. Garst, M., Waizner, J. & Grundler, D. Collective spin excitations of helices and magnetic skyrmions: review and perspectives of magnonics in non-centrosymmetric magnets. *J. Phys. D. Appl. Phys.* **50**, 293002 (2017).

38. Onose, Y., Okamura, Y., Seki, S., Ishiwata, S. & Tokura, Y. Observation of Magnetic Excitations of Skyrmion Crystal in a Helimagnetic Insulator Cu2OSeO3. *Phys. Rev. Lett.* **109**, 037603 (2012).

39. Schwarze, T. *et al.* Universal helimagnon and skyrmion excitations in metallic, semiconducting and insulating chiral magnets. *Nat. Mater.* **14**, 478–483 (2015).

40. Aqeel, A. *et al.* Microwave Spectroscopy of the Low-Temperature Skyrmion State in Cu2OSeO3. *Phys. Rev. Lett.* **126**, 017202 (2021).

41. Satywali, B. *et al.* Microwave resonances of magnetic skyrmions in thin film multilayers. *Nat. Commun.* **12**, 1909 (2021).

42. Srivastava, T. *et al.* Resonant dynamics of three-dimensional skyrmionic textures in thin film multilayers. *APL Mater.* **11**, 061110 (2023).

43. Luo, S. *et al.* Voltage-Controlled Skyrmion Memristor for Energy-Efficient Synapse Applications. *IEEE Electron Device Lett.* **40**, 635–638 (2019).

44. Kent, N. *et al.* Creation and observation of Hopfions in magnetic multilayer systems. *Nat. Commun.* **12**, 1562 (2021).

45. Zheng, F. *et al.* Hopfion rings in a cubic chiral magnet. *Nature* **623**, 718–723 (2023).

46. Tulapurkar, A. A. *et al.* Spin-torque diode effect in magnetic tunnel junctions. *Nature* **438**, 339–342 (2005).

47. Finocchio, G. *et al.* Perspectives on spintronic diodes. *Appl. Phys. Lett.* **118**, (2021).

48. Duong, N. K. *et al.* Stabilizing zero-field skyrmions in Ir/Fe/Co/Pt thin film multilayers by magnetic history control. *Appl. Phys. Lett.* **114**, 072401 (2019).

49. Tomasello, R. *et al.* Origin of temperature and field dependence of magnetic skyrmion size in ultrathin nanodots. *Phys. Rev. B* **97**, 060402 (2018).

50. Giordano, A., Finocchio, G., Torres, L., Carpentieri, M. & Azzerboni, B. Semi-implicit integration scheme for Landau–Lifshitz–Gilbert-Slonczewski equation. *J. Appl. Phys.* **111**, 07D112 (2012).

51. Alejos, O. *et al.* Current-driven domain wall dynamics in ferromagnetic layers synthetically exchange-coupled by a spacer: A micromagnetic study. *J. Appl. Phys.* **123**, 013901 (2018).

52. Darwin, E. *et al.* Antiferromagnetic interlayer exchange coupled Co68B32/Ir/Pt multilayers. *Sci. Rep.* **14**, 95 (2024).

53. Siracusano, G. *et al.* Micromagnetic simulations of persistent oscillatory modes excited by spin-polarized current in nanoscale exchange-biased spin valves. *J. Appl. Phys.* **105**, 07D107 (2009).

54. Cao, A. *et al.* Tuning the Dzyaloshinskii–Moriya interaction in Pt/Co/MgO heterostructures through the MgO thickness. *Nanoscale* **10**, 12062–12067 (2018).

Acknowledgements

R.T., M.C., E.D., and G.F. thank the projects PRIN 2020LWPKH7 “The Italian factory of micromagnetic modelling and spintronics”, PRIN20222N9A73 “SKYrmion-based magnetic tunnel junction to design a temperature SENSor—SkySens", funded by the Italian Ministry of Research, and the project number 101070287—SWAN-on-chip—HORIZON-CL4- 2021-DIGITAL EMERGING-01. R.T., M.C., E.D., and G.F. are with the Petaspin TEAM and thank the support of the PETASPIN association (www. petaspin.com). R.T. and M.C. acknowledge support from the Project PE0000021, “Network 4 Energy Sustainable Transition – NEST”, funded by the European Union – NextGenerationEU, under the National Recovery and Resilience Plan (NRRP), Mission 4 Component 2 Investment 1.3 - Call for tender No. 1561 of 11.10.2022 of Ministero dell’Università e della Ricerca (MUR) (CUP C93C22005230007). Z.Z. would like to acknowledge the National Natural Science Foundation of China (No. 52371206) and K. C. Wong Education Foundation (No. GJTD-2019-14). B. F. acknowledges support by the CAS Young Talent program. We also thank the Truth Instruments Co.ltd for the help in MOKE Characterizations.